A modified Fresnel-based algorithm for 3D microwave imaging of metal objects

Farshad Zamiri and Abdolreza Nabavi

Faculty of Electrical and Computer Eng., Tarbiat Modares University, Tehran, Iran

Abstract

Microwave holography technique reconstructs a target image using recorded amplitudes and phases of the signals reflected from the target with Fast Fourier Transform (FFT)-based algorithms. The reconstruction algorithms have two or more steps of two- and three-dimensional Fourier transforms, which have a high computational load. In this paper, by neglecting the impact of target depth on image reconstruction, an efficient Fresnel-based algorithm is proposed, involving only one-step FFT for both single- and multi-frequency microwave imaging. Numerous tests have been performed to show the effectiveness of the proposed algorithm including planar and non-planar targets, using the raw data gathered by means of a scanner operating in X-band. Finally, a low-cost and high-speed hardware architecture based on fixed-point arithmetic is introduced which reconstructs the planar targets. This pipeline architecture was tested on field programmable gate arrays operating at 200 MHz clock frequency, which illustrates more than 30 times improvement in computation time compared with a computer.

Introduction

Many methods have been developed using microwaves to detect concealed objects [1], based on modified optical holography and recording the interference pattern of a scattering target. Microwaves are able to penetrate clothes and reflect from the surface of a human body [2]. This property of microwaves provides the ability for concealed object detection such as metal (i.e. knives, handguns), plastic, and ceramic objects. In addition, commonly used systems including X-ray systems and metal detectors have some disadvantages. X-ray systems are not safe for human health [3]. Metal detectors can only detect metallic objects, and correct operation of these detectors depend on the quantity, orientation, and type of metal [2]. In addition, metal detectors have numerous wrong alarms because they are not capable to differentiate threatening and non-threatening objects (i.e. a bunch of keys, belt buckles), so it reduces the speed of detection. These reasons encourage using microwaves for detection.

For single-frequency imaging, the reconstructed image can be focused on only a single focal depth. However, in wideband frequency imaging, the focal depth can be extended by increasing the number of sampling frequencies, so the more frequency sampling points are, the more range resolution can be achieved [4].

In the past, numerous research works have been proposed for microwave imaging. A wide-bandwidth three-dimensional (3D) microwave holography was introduced in [2], and a 27–33 GHz imaging system was developed. In [5], three similar radars were designed in 3.6–4, 5.8–6.8, 14–15 GHz, and algorithms for the planar and circular apertures were outlined. A comparison between single-, two-, and multi-frequency sampling with subsurface holographic imaging system were carried out in [6] on simulated holograms and experimentally sampled holograms by means of a 3.9 GHz RASCAN radar. A fast imaging algorithm based on convolution technique was introduced and compared with Kirchhoff migration technique in [7]. This algorithm was able to reconstruct the image in a short time. In addition, to experimentally test the algorithm, a synthetic aperture radar in 5–25 GHz was utilized to obtain a 3D image of a knife and a gun. Another processing technique based on signal accumulation for microwave imaging was proposed for a moving target in [8], and two radars, operating at frequency bandwidth of 6.4–6.8 and 13.8–14.6 GHz, have been built to acquire the raw data. In [9], a new method for reconstructing the radar image from the intensity of sampled data was proposed, which led to a simple hardware implementation and a decrease in imaging system cost. A 92–94 GHz radar based on stepped-frequency pulse signal was used to record raw data, and 3D image reconstruction based on wave number domain algorithm was carried out in [10]. In [11] an amplitude correction of the algorithm in [2] was done in addition to building a holographic imaging system, which operates at 28–33 GHz. Recently, an algorithm based on wave-front reconstruction theory [12] has been developed, which was tested by means of a wide-band imaging system operating in Ka-band.

This paper presents an efficient image reconstruction algorithm based on Fresnel approximation, which only requires a single step of Fast Fourier Transform (FFT). This algorithm

reconstructs 2D and 3D targets by means of the data acquired over a scanning surface operating in 8–12 GHz. Numerous targets (i.e. copper, aluminum, metal, and plastic) have been tested to examine the effectiveness of the algorithm. Finally, a prototype hardware architecture is proposed to speed up the reconstruction. This hardware is tested on a field programmable gate array (FPGA) with 200 MHz clock rate.

Algorithms

Single-frequency reconstruction algorithm

In this section, a new single-frequency algorithm is presented for holographic imaging. Figure 1 depicts the recording method for microwave holography. The wave is emitted from a transmitter (*Tx*) antenna, and after reflection from the target, it is received by a receiver (*Rx*) antenna placed right beside the *Tx* antenna. Raster scanning is done for the recording process.

Assume the transmitter and receiver (transceiver) antennas in Fig. 1 are at point $(x, y, 0)$, and (ξ, η, d) denotes a point on the target plane. Here d represents the distance between the scanned plane and the target plane. The target is assumed to be defined by a reflectivity function $\Gamma(\xi, \eta)$, described by the ratio of the reflected field and the incident field [2]. The received signal $h(x, y)$ on the scanned aperture, which is related to the target's reflectivity function, is given by Equation (1) and ρ is defined by Equation (2). To obtain the reconstruction formula, it is necessary to derive $\Gamma(\xi, \eta)$ in terms of $h(x, y)$.

$$h(x, y) = \int_{-\infty}^{\infty} \int_{-\infty}^{\infty} \Gamma(\xi, \eta) \exp\left(-2i \frac{2\pi}{\lambda} \rho\right) d\xi d\eta, \quad (1)$$

$$\rho = \sqrt{(x - \xi)^2 + (y - \eta)^2 + d^2}. \quad (2)$$

λ is the wavelength and ρ denotes the distance between a general point in the scanned plane and the target plane. Here, by using a first-order Taylor series expansion of Equation (2) and by neglecting the effect of signal phase-shift, we will show that sufficient accuracy is obtained in our imaging algorithm. However, in optical communications where wave mixing occurs, this approximation may not be proper, and higher orders of Taylor series expansion are needed [13, 14].

Equation (2) can be expanded to first-order Taylor series, and after simplification based on Fresnel approximation ρ can be rewritten, as given below.

$$\rho = d + \frac{(\xi - x)^2}{2d} + \frac{(\eta - y)^2}{2d}. \quad (3)$$

By substituting ρ from Equation (3) in Equation (1) and after re-arranging, we have:

$$h(x, y) = \exp\left(-2i \frac{2\pi}{\lambda} d\right) \exp\left(-i \frac{2\pi}{\lambda d}(x^2 + y^2)\right)$$
$$\times \int_{-\infty}^{\infty} \int_{-\infty}^{\infty} \Gamma(\xi, \eta) \exp\left(-i \frac{2\pi}{\lambda d}(\xi^2 + \eta^2)\right) \quad (4)$$
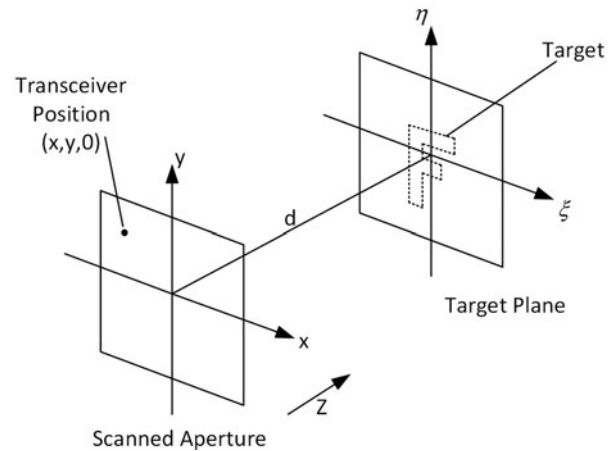$$\times \exp\left(2i \frac{2\pi}{\lambda d}(x\xi + y\eta)\right) d\xi d\eta.$$

Fig. 1. 2D coordinate system for microwave holography.

We employ two new factors defined as:

$$v = \frac{2x}{\lambda d}; \quad \mu = \frac{2y}{\lambda d}. \quad (5)$$

Hence, Equation (4) may be shown as:

$$h(v, \mu) = \exp\left(-i \frac{4\pi}{\lambda} d\right) \exp\left(-i \frac{\pi \lambda d}{2}(v^2 + \mu^2)\right)$$
$$\times \int_{-\infty}^{\infty} \int_{-\infty}^{\infty} \Gamma(\xi, \eta) \exp\left(-i \frac{2\pi}{\lambda d}(\xi^2 + \eta^2)\right) \quad (6)$$
$$\times \exp(i2\pi(\xi v + \eta \mu)) d\xi d\eta$$

Based on Fourier transform definition, the integrals in Equation (6) are 2D inverse Fourier transform (IFT) of $\Gamma(\xi, \eta) \exp(-i2\pi (\xi^2 + \eta^2)/\lambda d)$. Thus:

$$h(v, \mu) \exp\left(i \frac{4\pi}{\lambda} d\right) \exp\left(i \frac{\pi \lambda d}{2}(v^2 + \mu^2)\right)$$
$$= FT_{2D}^{-1}\left[\Gamma(\xi, \eta) \exp\left(-i \frac{2\pi}{\lambda d}(\xi^2 + \eta^2)\right)\right]. \quad (7)$$

The term $\exp(i4\pi d/\lambda)$ can be omitted because it only yields a phase shift and it has no impact on the amplitude of the reconstructed image. After taking 2D Fourier transform from each side of Equation (7), the new equation will be:

$$\Gamma(\xi, \eta) \exp\left(-i \frac{2\pi}{\lambda d}(\xi^2 + \eta^2)\right)$$
$$= FT_{2D}\left[h(v, \mu) \exp\left(i \frac{\pi \lambda d}{2}(v^2 + \mu^2)\right)\right]. \quad (8)$$

The exponential term in the left side of the above equation can be ignored because its impact is only a phase shift in the reconstructed image. Note that for the microwave imaging, the phase shift has no impact on image intensity. The reason is that, as described by Equation (14) below, the intensity is defined as the absolute value of $\Gamma(\xi, \eta)$, and it is known from basic mathematics that the exponential term has unity absolute value. Thus, the

reconstruction formula is:

$$\Gamma(\xi, \eta) = FT_{2D}\left[h(\nu, \mu)\exp\left(i\frac{4\pi}{\lambda}d\right)\exp\left(i\frac{\pi\lambda d}{2}(\nu^2 + \mu^2)\right)\right]$$

$$= \int_{-\infty}^{\infty}\int_{-\infty}^{\infty}h(\nu, \mu)\exp\left(i\frac{\pi\lambda d}{2}(\nu^2 + \mu^2)\right)$$

$$\times \exp(-i2\pi(\xi\nu + \eta\mu))d\nu d\mu$$

$$(9)$$

where $h(\nu, \mu)$ is the recorded hologram, which should be defined in terms of (x, y). Thus, based on Equation (5) we have:

$$\nu = \frac{2x}{\lambda d} \rightarrow d\nu = \frac{2}{\lambda d}dx$$

$$\mu = \frac{2y}{\lambda d} \rightarrow d\mu = \frac{2}{\lambda d}dy,$$

$$(10)$$

$$\Gamma(\xi, \eta) = \frac{4}{\lambda^2 d^2}\int_{-\infty}^{\infty}\int_{-\infty}^{\infty}h(x, y)\exp\left(i\frac{2\pi}{\lambda d}(x^2 + y^2)\right)$$

$$\times \exp\left(-i2\pi\left(\frac{2}{\lambda d}\right)(\xi x + \eta y)\right)dxdy$$

$$(11)$$

The term $4/\lambda^2 d^2$ can be omitted because it is only a constant coefficient without any effect on the resulted image. Assume ν' and μ' are defined as:

$$\nu' = \frac{2\xi}{\lambda d}; \quad \mu' = \frac{2\eta}{\lambda d}.$$

$$(12)$$

Therefore, the reconstruction formula is summarized by:

$$\Gamma(\nu', \mu') = \int_{-\infty}^{\infty}\int_{-\infty}^{\infty}h(x, y)\exp\left(i\frac{2\pi}{\lambda d}(x^2 + y^2)\right)$$

$$\times \exp(-i2\pi(x\nu' + y\mu'))dxdy$$

$$(13)$$

A comparison of Equation (13) with 2D Fourier transform shows that the integrals are Fourier transform of $h(x, y)\exp(i(2\pi/\lambda d)(x^2 + y^2))$.

The intensity of the image is calculated by the following Equation [15]:

$$I(\nu', \mu') = |\Gamma_{\nu', \mu'}|^2,$$

$$(14)$$

where $I(\nu', \mu')$ represents the intensity function.

Multi-frequency reconstruction algorithm

This section describes the proposed multi-frequency algorithm for 3D image reconstruction. Figure 2 shows the coordinate system for 3D microwave holography. A raster scan is performed to record the raw data. For each sampling point (x, y, z_0), the receiver antenna samples data with the desired frequency bandwidth. Also, (ξ, η, z) is a general point on the target, which is placed in front of the scanned plane in an imaginary test cube with dimensions defined in relation to the scanning plane size in horizontal and vertical axis, and the frequency bandwidth.

Assume $\Gamma(\xi, \eta, z)$ is the target reflectivity function [2]. The received signal $h(x, y, f)$ on the scanned aperture is related to the target reflectivity function, as given by Equation (15), and ρ
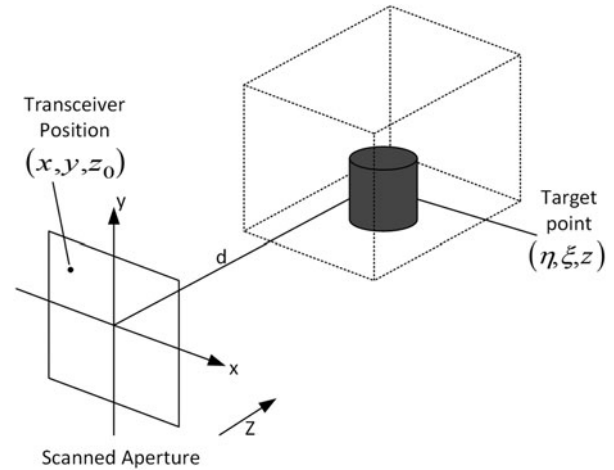

Fig. 2. 3D coordinate system for microwave holography.

is defined by Equation (16). Our goal is to derive $\Gamma(\xi, \eta, z)$ in terms of $h(x, y, f)$ as the reconstruction formula.

$$h(x, y, f) = \iiint \Gamma(\xi, \eta, z)\exp\left(-2i\frac{2\pi}{\lambda}\rho\right)d\xi d\eta dz,$$

$$(15)$$

$$\rho = \sqrt{(x - \xi)^2 + (y - \eta)^2 + (z - z_0)^2},$$

$$(16)$$

where λ is the wavelength, and ρ is the distance between a point in the scanned plane and the target plane.

Similarly, as described for Equation (2), by expanding Equation (16) to first-order Taylor series and based on Fresnel approximation, Equation (16) can be simplified as:

$$\rho = (z - z_0) + \frac{(\xi - x)^2 + (\eta - y)^2}{2(z - z_0)}$$

$$= \frac{2(z - z_0)^2 + (\xi - x)^2 + (\eta - y)^2}{2(z - z_0)}$$

$$= z - \frac{zz_0 + \xi x + \eta y}{d} + \frac{\xi^2 + \eta^2}{2d} + \frac{x^2 + y^2}{2d} + \frac{z_0^2}{d}.$$

$$(17)$$

In Equation (17), the term $(z - z_0)$ in the denominator can be replaced by d if the target depth is small compared with d.

By substituting ρ from Equation (17) in Equation (15) and re-arranging, we obtain:

$$h(x, y, f) = \exp\left(-2i\frac{2\pi}{\lambda}\frac{z_0^2}{d}\right)\exp\left(-i\frac{2\pi}{\lambda d}(x^2 + y^2)\right)$$

$$\times \iiint \Gamma(\xi, \eta, z)\exp\left[-2i\left(\frac{2\pi}{\lambda}\right)z\right]$$

$$\times \exp\left(-i\frac{2\pi}{\lambda d}(\xi^2 + \eta^2)\right)$$

$$\times \exp\left(2i\frac{2\pi}{\lambda d}(zz_0 + x\xi + y\eta)\right)d\xi d\eta dz.$$

$$(18)$$

We employ two new factors defined as:

$$v = \frac{2x}{\lambda d}; \quad \mu = \frac{2y}{\lambda d}; \quad \gamma = \frac{2z_0}{\lambda d} . \tag{19}$$

By substituting the above parameters in Equation (18), we achieve:

$$
\begin{aligned}
h(v, \mu, \gamma) = {}& \exp(-i\pi\lambda d\gamma^2) \exp\left(-i\frac{\pi\lambda d}{2}(v^2 + \mu^2)\right) \\
& \times \iiint \Gamma(\xi, \eta, z) \exp\left[-2i\left(\frac{2\pi}{\lambda}\right)z\right] \\
& \times \exp\left(-i\frac{2\pi}{\lambda d}(\xi^2 + \eta^2)\right) \\
& \times \exp(i2\pi(z\gamma + \xi v + \eta\mu))d\xi d\eta dz.
\end{aligned}
\tag{20}
$$

By re-ordering the equation and comparing integrals with the inverse 3D Fourier transform, Equation (20) can be changed to:

$$
\begin{aligned}
h(v, \mu, \gamma) & \exp(i\pi\lambda d\gamma^2) \exp\left(i\frac{\pi\lambda d}{2}(v^2 + \mu^2)\right) \\
& = FT_{3D}^{-1}\left[\Gamma(\xi, \eta, z) \exp\left[-2i\left(\frac{2\pi}{\lambda}\right)z\right]\right. \\
& \quad \left. \times \exp\left(-i\frac{2\pi}{\lambda d}(\xi^2 + \eta^2)\right)\right].
\end{aligned}
\tag{21}
$$

After taking 3D Fourier transform from each side of Equation (21), and by omitting the exponential terms of the right side, which are only a phase shift in the reconstructed image without impact on the intensity of the image, this equation will be:

$$
\begin{aligned}
\Gamma(\xi, \eta, z) = FT_{3D}[& h(v, \mu, \gamma) \exp(i\pi\lambda d\gamma^2) \\
& \times \exp\left(i\frac{\pi\lambda d}{2}(v^2 + \mu^2)\right)],
\end{aligned}
\tag{22}
$$

where $h(v, \mu, \gamma)$ is the recorded hologram, which may be defined in terms of (x, y, f). As described before, exponential terms have unity absolute value, so they have no impact on intensity, and can be omitted in Equation (21), where the intensity is of interest. Thus, based on Equation (19), we have:

$$
\begin{aligned}
v &= \frac{2x}{\lambda d} \rightarrow dv = \frac{2}{\lambda d}dx \\
\mu &= \frac{2y}{\lambda d} \rightarrow d\mu = \frac{2}{\lambda d}dy \\
\gamma &= \frac{2z_0}{\lambda d} \rightarrow d\gamma = \frac{2z_0}{cd}df,
\end{aligned}
\tag{23}
$$

$$
\begin{aligned}
\Gamma(\xi, \eta, z) = {}& \frac{8z_0}{\lambda^2 d^3 c} \iiint h(x, y, f) \exp\left(i\frac{4\pi z_0^2}{cd}f\right) \\
& \times \exp\left(i\frac{2\pi}{\lambda d}(x^2 + y^2)\right) \\
& \times \exp\left(-i2\pi\left(\frac{2}{\lambda d}\right)(x\xi + y\eta + zz_0)\right)dxdydf.
\end{aligned}
\tag{24}
$$

Frequency f can be represented by a differential frequency f_d from the center frequency f_c, so $f = f_c + f_d$. If $f_c \gg f_d$ then f_d can be omitted [16]. Based on this approximation, Equation (24) is rewritten as:

$$
\begin{aligned}
\Gamma(\xi, \eta, z) = \iiint & h(x, y, f) \exp\left(i\frac{2\pi}{\lambda d}(x^2 + y^2)\right) \\
& \times \exp\left(-i2\pi\left(\frac{2f_c}{cd}x\xi + \frac{2f_c}{cd}y\eta + \frac{2z_0}{cd}fz\right)\right)dxdydf.
\end{aligned}
\tag{25}
$$

To finalize the reconstruction formula, again we assume that:

$$
\begin{aligned}
v' &= \frac{2f_c}{cd}\,\xi \\
\mu' &= \frac{2f_c}{cd}\,\eta \\
\gamma' &= \frac{2z_0}{cd}z.
\end{aligned}
\tag{26}
$$

Thus, the reconstruction formula for multi-frequency microwave holography is:

$$
\begin{aligned}
\Gamma(v', \mu', \gamma') = \iiint & h(x, y, f) \exp\left(i\frac{2\pi}{\lambda d}(x^2 + y^2)\right) \\
& \times \exp(-i2\pi(xv' + y\mu' + f\,\gamma'))dxdydf.
\end{aligned}
\tag{27}
$$

Clearly, in Equation (27) the integrals are 3D Fourier transform of $h(x, y, f)\exp(i(2\pi/\lambda d)(x^2 + y^2))$.

Algorithm digitization

This section introduces the digitized versions of single- and multi-frequency reconstruction algorithms for microwave holography. Recorded hologram h is discretized in transceiver plane. Therefore, a digitized representation of the proposed algorithm is required. For the single-frequency algorithm, assume that the sampled raw data $h(x, y)$ is a $N \times N$ matrix with physical space Δx and Δy in x- and y-directions, respectively. Thus, integrals in Equation (13) will change to finite sums of:

$$
\begin{aligned}
\Gamma(m, n) = \sum_{l=0}^{N-1}\sum_{k=0}^{N-1} & h(k, l) \exp\left(i\frac{2\pi}{\lambda d}(k^2\Delta x^2 + l^2\Delta y^2)\right) \\
& \times \exp(-i2\pi(k\Delta x.m\Delta v' + l\Delta y.n\Delta\mu')).
\end{aligned}
\tag{28}
$$

Based on Fourier transform theory, between $(\Delta x, \Delta y)$ and $(\Delta v', \Delta \mu')$ the following relations exist:

$$\Delta v' = \frac{1}{N\Delta x}; \quad \Delta\mu' = \frac{1}{N\Delta y}. \tag{29}$$

After re-substitution:

$$\Delta\xi = \frac{\lambda d}{2N\Delta x}; \quad \Delta\mu = \frac{\lambda d}{2N\Delta y}. \tag{30}$$

Using the above expressions, Equation (28) is converted to

Equation (31).

$$\Gamma(m, n) = \sum_{l=0}^{N-1} \sum_{k=0}^{N-1} h(k, l) \exp\left(i\frac{2\pi}{\lambda d}(k^2\Delta x^2 + l^2\Delta y^2) \right)$$
$$\times \exp\left(-i2\pi\left(\frac{km}{N} + \frac{ln}{N}\right) \right). \tag{31}$$

This equation is the digitized version of the proposed single-frequency reconstruction algorithm. With a comparison of Equation (31) by discrete 2D Fourier transform definition, the summations are the Fourier transform of $h(k, l)\exp(i(2\pi/\lambda d)$ $(k^2\Delta x^2 + l^2\Delta y^2))$.

For the multi-frequency algorithm, assume that the sampled raw data $h(x, y, f)$ is a $N \times N \times N_f$ matrix with physical space Δx, Δy in x- and y-directions, respectively, and with frequency space of Δf. Therefore, integrals in Equation (27) may be changed to finite sums of:

$$\Gamma(m, n, q) = \sum_{p=0}^{N_f-1} \sum_{l=0}^{N-1} \sum_{k=0}^{N-1} h(k, l, p)$$
$$\times \exp\left(i\frac{2\pi p\Delta f}{cd}(k^2\Delta x^2 + l^2\Delta y^2) \right)$$
$$\times \exp(-i2\pi(k\Delta x.m\Delta\nu' + l\Delta y.n\Delta\mu' + p\Delta f.q\Delta\gamma')). \tag{32}$$

Based on Fourier transform theory, between $(\Delta x, \Delta y, \Delta f)$ and $(\Delta\nu', \Delta\mu', \Delta\gamma')$ the following relations exist:

$$\Delta\nu' = \frac{1}{N\Delta x}; \quad \Delta\mu' = \frac{1}{N\Delta y}; \quad \Delta\gamma' = \frac{1}{N_f\Delta f}. \tag{33}$$

After re-substitution:

$$\Delta\xi = \frac{\lambda d}{2N\Delta x}; \quad \Delta\mu = \frac{\lambda d}{2N\Delta y}; \quad \Delta z = \frac{cd}{2z_0 N_f\Delta f}. \tag{34}$$

Using the above expressions, Equation (32) is converted to:

$$\Gamma(m, n, q) = \sum_{p=0}^{N_f-1} \sum_{l=0}^{N-1} \sum_{k=0}^{N-1} h(k, l, p)$$
$$\times \exp\left(i\frac{2\pi p\Delta f}{cd}(k^2\Delta x^2 + l^2\Delta y^2) \right) \tag{35}$$
$$\times \exp\left(-i2\pi\left(\frac{km}{N} + \frac{ln}{N} + \frac{pq}{N_f}\right) \right).$$

Equation (35) is the digitized version of the proposed multi-frequency reconstruction algorithm. In Equation (35), Fourier transform of $h(k, l)\exp(i(2\pi/\lambda d)(k^2\Delta x^2 + l^2\Delta y^2))$ is the result of summations.

Experimental setup

A 2D electro-mechanical scanner was built to record raw data of the hologram. A controller board, connected to the USB port of a PC, was used to control the motion of the scanner in horizontal and vertical directions. The PC was used to set up the microcontroller moving with the given steps. A PNA Microwave Network Analyzer was utilized to record the amplitude and phase of the received waves, by means of two horn antennas one as a transmitter and the other as a receiver. This setup is able to scan a $N \times N \times N_f$ matrix in X-band frequency with any sampling intervals. Due to mechanical constraints, the scanned plane can be the maximum size of 32 cm × 32 cm, and the targets were placed in the distance of 18.5 cm from the transmitter and receiver pairs. The target was hung from the ceiling to neutralize the vibration produced by the movement of the scanner motors. The controller board is presented in Fig. 3, and the transmitter and receiver antenna pairs are shown in Fig. 4. In addition, the test environment can be observed in Fig. 5. In order to control the background reflected wave, absorbers are placed behind the targets.

Laboratory scanned imaging results

In this section, we examine the effectiveness of the proposed algorithm by performing some tests and reporting the reconstructed images. The target distance from the antennas was $d = 18.5$ cm. A 10 GHz wave was transmitted to the targets, which was scanned in a plane surface of 32 cm × 32 cm with sampling step sizes of $\Delta x = \Delta y = 1$ cm in both X and Y directions. The amplitude and phase of the reflected wave were recorded. Then, the processing algorithm described in the sections Single-frequency reconstruction algorithm and Multi-frequency reconstruction algorithm reconstructs the meaningful picture.

Our experimental tests showed that in order to properly reconstruct the picture, the scan plane dimensions must be approximately twice of the target dimensions. This was tested experimentally. As a result, the target maximum size could be approximately 16 cm × 16 cm because we can scan a maximum plane size of 32 cm × 32 cm.

In order to enhance the signal-to-clutter ratio, the background was scanned and subtracted from the target raw holograms [1]. This technique removes the effect of reflections from non-ideal absorbers and other existing objects in the room, which improves the quality of the image. In addition, background subtraction reduces the effect of mutual coupling of the antennas [17]. Nevertheless, our tests show that subtracting the background only slightly improves the resolution of the reconstructed image, because the mutual coupling between antennas was low and the reflected wave was weak since the background was relatively far from the target. However, when the target is near the background, the above subtraction may be necessary.

Two planar objects were tested based on the above setup. A copper F shape target was designed with dimensions of 11 cm × 17 cm in X- and Y-axis, respectively. Also, another aluminum wrapped Γ shape target was placed in front of the 3D scanner to test the proposed single-frequency algorithm. The dimensions of this target are 16 cm × 16 cm. The targets are illustrated in Fig. 6, and the raw hologram and reconstructed images are shown in Figs 7 and 8 for F shape and Γ shape targets, respectively. The proposed single-frequency algorithm was used to process the raw hologram and to reconstruct the images.

In addition, a 64 × 64 image, with sampling intervals of 0.5 cm in both X and Y directions, is sampled from the same target in Fig. 6(b). The raw data matrix and the reconstructed image are shown in Fig. 9.

Furthermore, the scan of the same object is done with sampling intervals of 1 cm in each direction at 11 GHz frequency.
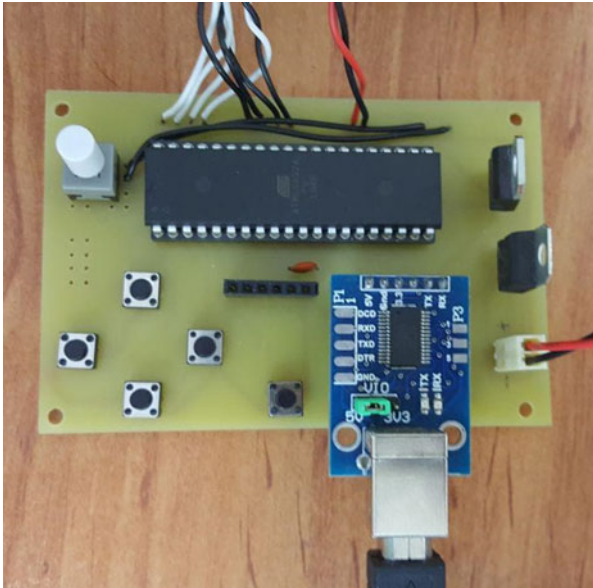
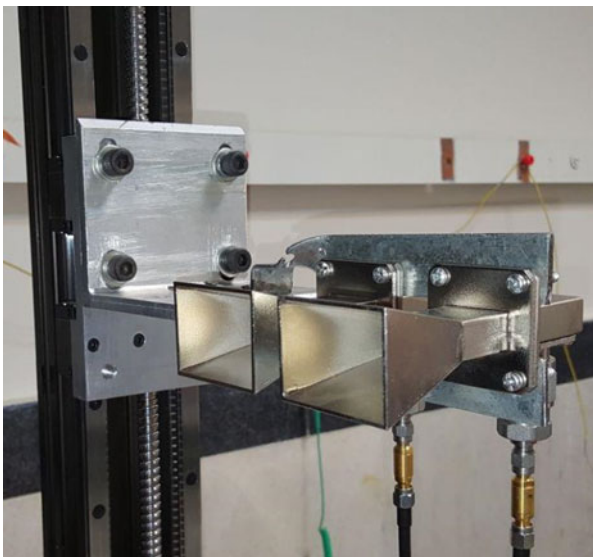**Fig. 3.** Designed controller board to control the mechanical movement of the scanner.

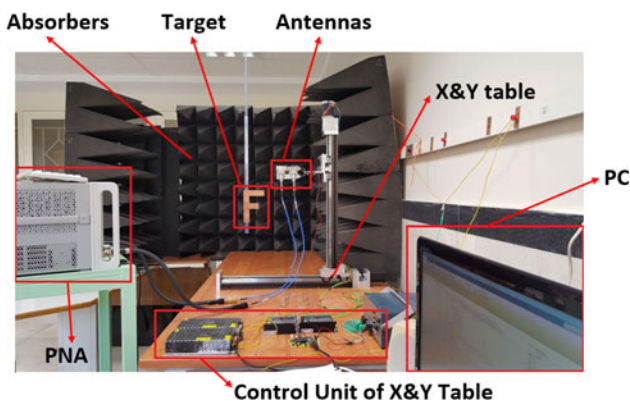

Fig. 4. Transmitter and receiver horn antennas.
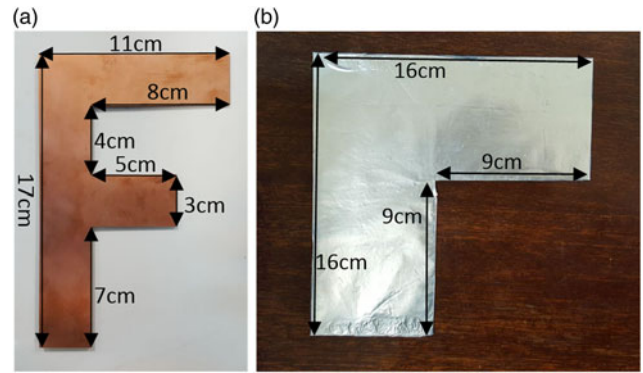

Fig. 5. Test environment.

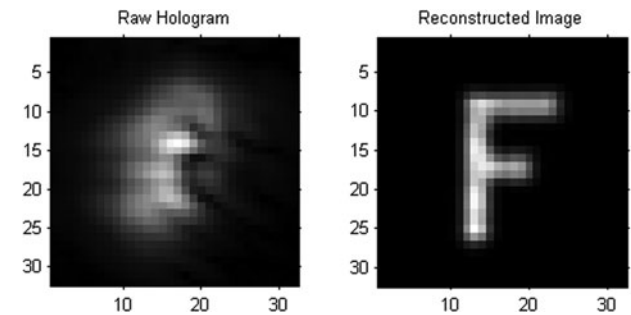**Fig. 6.** (a) Copper F shaped flat target (b) Aluminum wrapped Γ shape flat target.

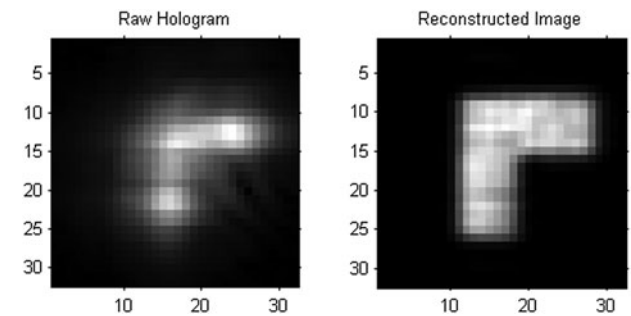**Fig. 7.** Raw hologram and reconstructed image of F shape target (10 GHz).

Fig. 8. Raw hologram and reconstructed image of Γ shape target (10 GHz) (32 × 32 image).

The raw hologram and the reconstructed image are illustrated in Fig. 10.

Another test has been done to examine the capability of the single-frequency algorithm to reconstruct a scene containing multi-objects. In this measurement, a 10 cm × 6 cm rectangular aluminum target, a 3 cm and a 2 cm diameter coins are placed in the target plane. The space between the objects is 2.7 cm, and the target scene is shown in Fig. 11. By performing the proposed algorithm on the raw data matrix, the reconstructed image can be observed in Fig. 12. The rectangular target has been reconstructed successfully. Because of large step of antenna movement ($\Delta x = \Delta y = 1$ cm) compared with the diameter of coins (2 cm and 3 cm), and the fact that the small coins must be shown in a 32 × 32 pixel image (each pixel is about 1 cm × 1 cm), it is slightly hard to diagnose the circular shape of the coins. However, it can be observed that one of the coins is smaller than the other one in the resulted image.
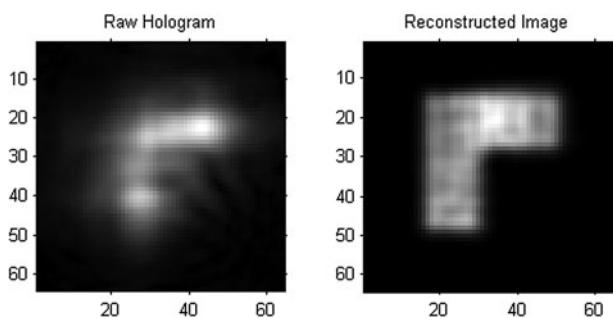
Fig. 9. Raw hologram and reconstructed image of Γ shape target (10 GHz) (64 × 64 image).

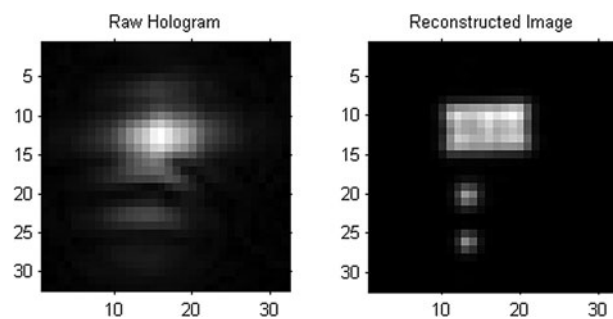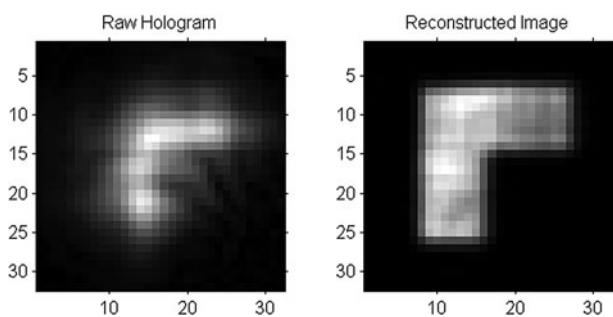**Fig. 10.** Raw hologram and reconstructed image of Γ shape target (11 GHz).
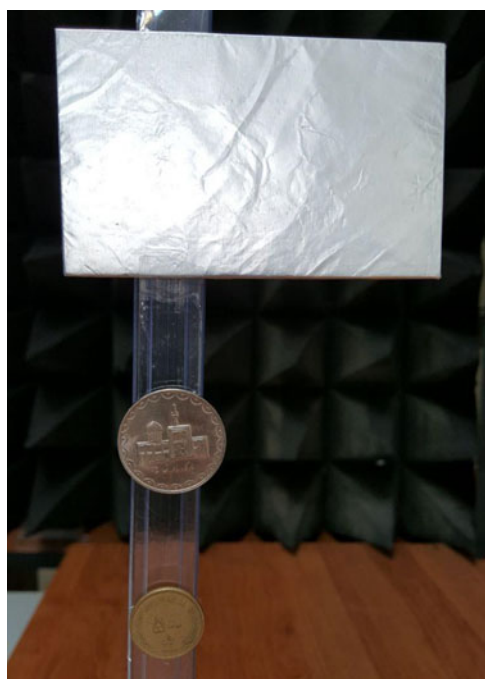

Fig. 11. Aluminum wrapped rectangular target and two coins.

To experimentally test the minimum cross-range resolution that may be obtained by the above setup, two aluminum rectangular shape targets were placed near each other. The processing algorithm was used to reconstruct the image of these two targets. Then, they were gradually moved closer until two reconstructed rectangles overlap. The minimum distance before which this

Fig. 12. Raw hologram and reconstructed image of the targets in Fig. 11.

overlap occurs is approximately the possible cross-range resolution in the target plane. The results of two tests are reported here. The first test was a 32 × 32 image with $\Delta x = \Delta y = 1$ cm, and the space of 1.5 cm. The target scene is shown in Fig. 13 (a), and the reconstructed image is shown in Fig. 14. In this case, no overlap is observed. The second test was a 128 × 128 image with $\Delta x = \Delta y = 0.25$ cm, and the space between two objects is about 0.9 cm. The target scene is shown in Fig. 13(b), and the reconstructed image is shown in Fig. 15. Here, the two rectangular objects are distinguishable. According to Equation (30), for 10 GHz wave and $d = 18.5$ cm, both $\Delta\xi$ and $\Delta\eta$ which define the resolution are 0.87 cm. Therefore, this resolution is experimentally verified for the proposed single-frequency reconstruction algorithm.

The F shape target in Fig. 6(a) is placed in the distance $d = 42$ cm, and the sampled frequency is again 10 GHz with $\Delta x = \Delta y = 1$ cm sampling intervals. The raw data and the reconstructed 32 × 32 image are illustrated in Fig. 16.

In order to test the proposed 3D reconstruction algorithm, the previously described scanner was used. This scanner is capable to record raw data in the frequency range of interest. The scanning process is the same as single-frequency recording, but the difference is that in each sampling point, instead of one frequency sample, a frequency sweep is performed. An 8–11.5 GHz scan with sampling intervals of $\Delta x = \Delta y = 2.5$ mm in both X and Y directions is carried out. The number of frequency points is 35 in the bandwidth, and the visual target, which is placed at the distance of 20 cm from the transceiver antennas, is represented in Fig. 17. The reconstructed image with the proposed multi-frequency algorithm is shown in Fig. 18. According to this picture, since metallic objects reflect the microwaves better than the plastic ones, scissor blades are brighter than the plastic ring handles.

Next, two spray bottles were placed in the test environment, which is illustrated in Fig. 19 for the multi-frequency algorithm verification. The reconstructed image of this complex target is shown in Fig. 20. The middle part of the targets in the reconstructed image is less bright than the other parts because it is farther from the scanning plane.

Hardware design

In previous sections, the system level test of the algorithm has been performed using MATLAB. In this section, a prototype hardware architecture based on FPGAs is introduced to increase the speed of the proposed algorithm computations. This prototype can process 32 × 32 raw holograms but can be expanded to reconstruct larger input matrices. It is also designed for the
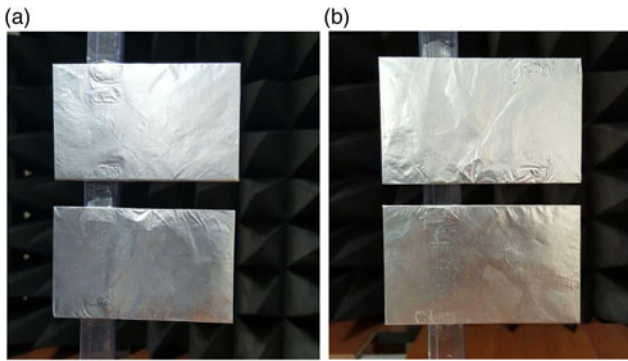
Fig. 13. Two wrapped aluminum rectangular shape with (a) 1.5 cm (b) 0.9 cm space in between.
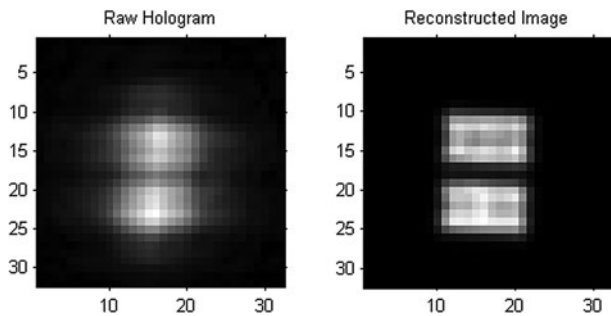

Fig. 14. Reconstructed image of two rectangular shape target of Fig. 13(a).
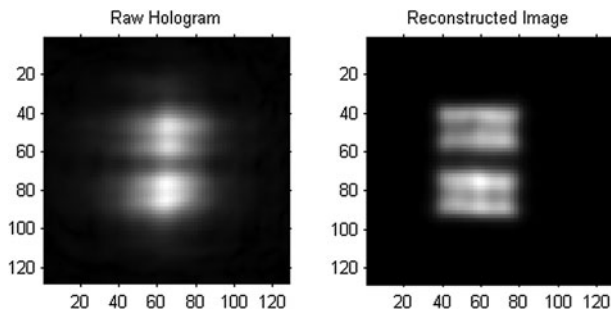

Fig. 15. Reconstructed image of two rectangular shape target of Fig. 13(b).
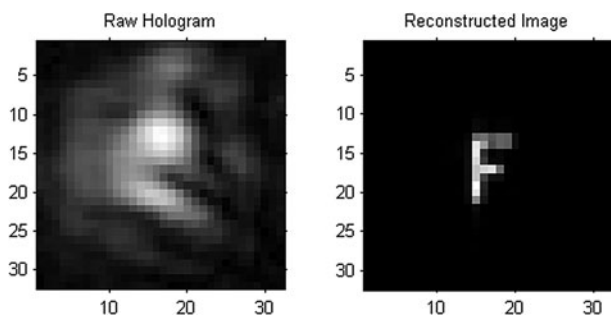

Fig. 16. Raw hologram and reconstructed image of the F shape target placed in the distance of 42 cm.

proposed 2D reconstruction algorithm, which can be adapted to have the ability to process 3D matrices of the proposed 3D reconstruction algorithm. To explain the designed architecture, we need

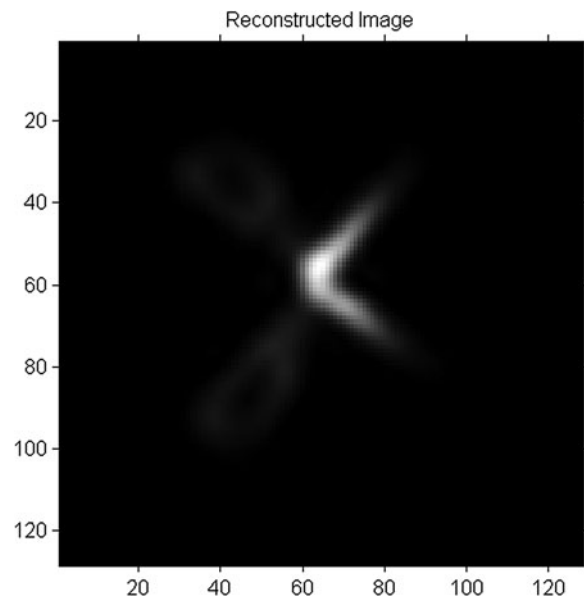**Fig. 17.** A scissor as the target for multi-frequency imaging.

Fig. 18. Reconstructed image of a scissor (8–11.5 GHz).

to re-define previous 2D reconstruction equations as follows:

$$\Gamma_{u,v} = \sum_{x=0}^{N-1} \sum_{y=0}^{N-1} [\eta_{x,y} e^{i.addr1}] e^{-i2\pi \left(\frac{xu}{N} + \frac{yv}{N}\right)}, \tag{36}$$

$$addr1 = \frac{2\pi}{\lambda d} \Delta_f^2 (x^2 + y^2). \tag{37}$$

As it is noted before, two summations in the above equation are 2D FT of $\eta_{x,y} e^{i.addr1}$, which can be implemented efficiently with FFT method. Fixed-point computation is used for all processes of the algorithm because of its simplicity than a floating-point based hardware. Therefore, the fewer resources of FPGA are utilized and the power consumption is lower, while the speed will be higher. The calculations are based on the 12-bit resolution as the fraction.

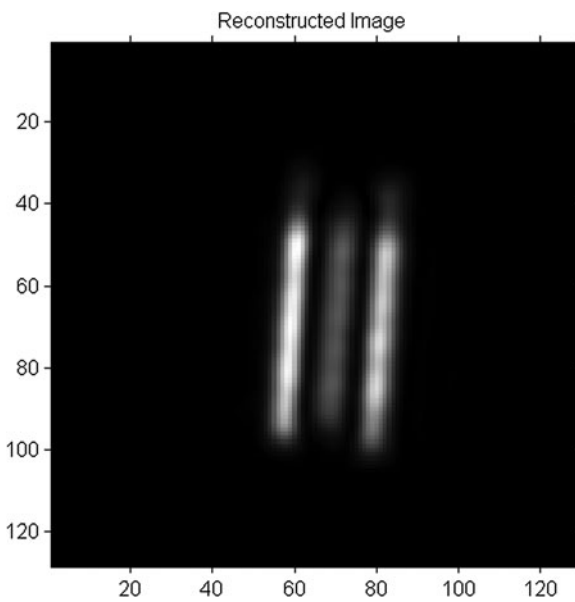**Fig. 19.** Two spray bottles as the target for multi-frequency imaging.

Fig. 21. Proposed architecture for the modified Fresnel-based algorithm.

Fig. 20. Reconstructed image of two spray bottles (8–11.5 GHz).

are used to compute the result of the following exponential function:

$$L_1 = e^{j.\text{addr1}}. \tag{38}$$

RAMs used for saving raw hologram $\eta_{x,y}$ are placed in the below-left block in Fig. 21. This block has also the role of shifting the zero-frequency component to the center of spectrum in the last part of the computation, which results in correct reconstructed image. In a matrix computation, this shift swaps the first quadrant of the matrix with the third, and the second quadrant with the fourth. The complex multiplier performs the operation of Equation (39).

$$\alpha = \eta_{x,y} \times L_1. \tag{39}$$

There is also a unit to compute 2D FFT (Equation (40)), and it has an internal controller to decrease load control of the main control unit. The main control unit shown in Fig. 21 controls the data flow of all units, and there are also some control signals to each block which are not shown in the picture to avoid bustling.

$$\Gamma_{u,v} = \Im = \sum_{x=0}^{N-1}\sum_{y=0}^{N-1}[\alpha]e^{-j2\pi\left(\frac{xu}{N}+\frac{yv}{N}\right)}. \tag{40}$$

As explained before, shifting the zero-frequency component to the center of the spectrum is the next operation that is needed to have a correct reconstructed image. Thus, after calculating $\Gamma_{u,v}$ or $\Im$, data moves to the next block to perform this shift. It should be noted that all blocks are disabled when they are not in use to save power consumption. In the following sections, sub-blocks of Fig. 21 will be described.

Architecture overview

The goal of the proposed architecture is to compute Equation (36) by introducing new hardware architecture to have an improvement in calculation time compared with a PC. The architecture is implemented on an FPGA to verify its correctness. To have a proper throughput, all parts of the proposed architecture are pipelined. Main units of the architecture are presented in Fig. 21. It has address generation unit (AGU), ROMs, RAMs, a complex multiplier and 2D FFT unit. AGU calculates addr1 in Equation (37). Next block contains a lookup table, which utilizes two ROMs to save real and imaginary parts of the required exponential term in Equation (36). Note that, to reduce the memory access time, all ROMs and RAMs are on-chip ones. This table is sampled and saved based on the required data range and resolution, which
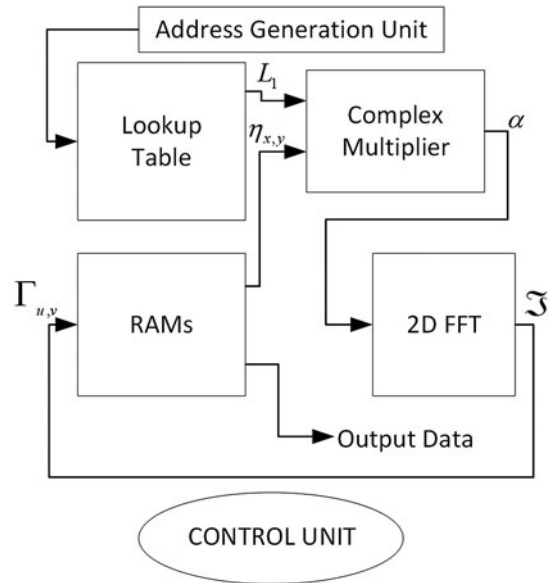
Address generation unit

The designed architecture for this unit is shown in Fig. 22. It makes the address in Equation (37) for the lookup table.
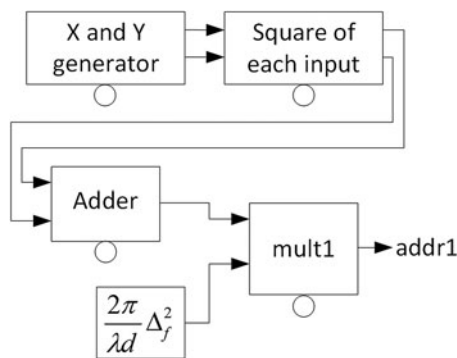
Fig. 22. Address generation unit.

Generating the address for the next block (ROMs) should be done in falling edges of the clock, so only this unit works with the falling edges of the clock signal.

When the circuit starts its operation, X and Y generator block starts to generate addr1. Since λ, d, and Δ_f are known, we save $(2\pi/\lambda d)\Delta_f^2$ as a constant coefficient in fixed-point format. Besides, X and Y generator block is responsible for generating X, Y indices. Square of each input block produces x^2 and y^2. Also, to obtain $x^2 + y^2$ an adder is placed in the path of data flow. Finally, the mult1 block performs the final operation to produce addr1 for the lookup table. Next block is the lookup table, and exponential terms are sampled and saved in certain steps, so the constant number is multiplied by the result to generate a suitable address for the lookup table.

It should be reminded that multiplication is done in fixed-point format, and then the required integer part is truncated to produce the address for the lookup table.

RAMs unit

This unit carries out two tasks in different time slots and contains an AGU, two RAMs, and a de-multiplexer. The first task is to save the real and imaginary parts of the raw hologram $\eta_{x,y}$ and to send it to the next block through de-multiplexer. This task is performed in the beginning of the process and in parallel with the block defined in the previous section. The second task is to shift the zero-frequency component to the center of the spectrum, which is performed in the final stage of reconstructing the image. The de-multiplexer is placed there to separate these two different tasks. Thus, in this block, AGU and two RAMs are shared in two different time slots to reduce the usage of FPGA resources. In this block, AGU generates the address needed to output the shifted form of the data Fig. 23.

2D FFT unit

The task of 2D FFT computation in Equation (40) is assigned to this unit, which includes 1D FFT block, two RAMs, a multiplexer, a de-multiplexer and an internal control unit. To calculate 2D FFT by means of 1D FFT, first FFT of the columns of the matrix is computed, and then FFT of the rows of the resulted matrix is obtained. Data are moved into the block continuously and column by column, and according to Fig. 24 the data are moved into 1D FFT block through the mux. The 1D FFT block operates in pipeline mode, so after certain latency, this block starts to output the results of FFT computation by each clock. Then these real and imaginary
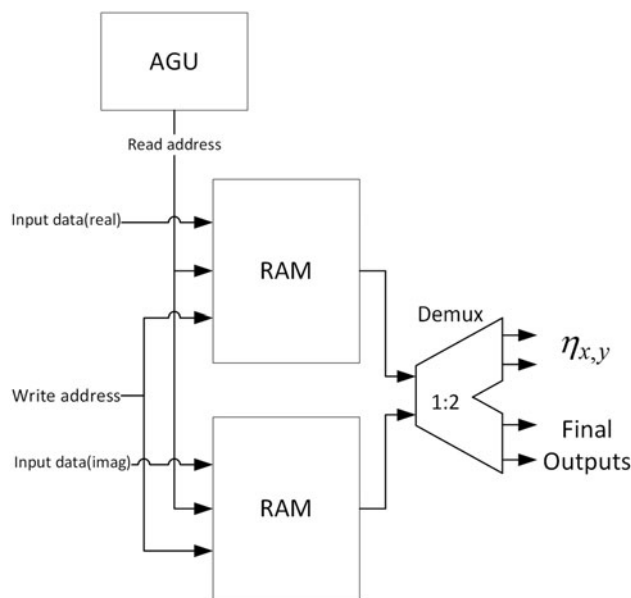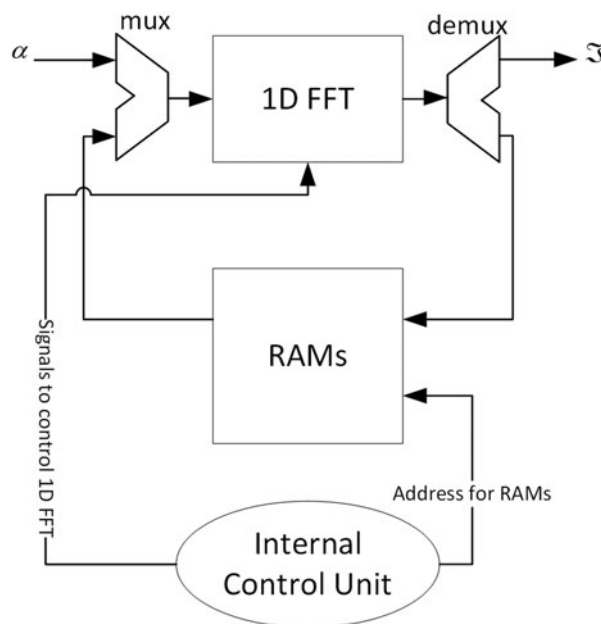

Fig. 23. Units of RAMs.

Fig. 24. 2D FFT block.

results are saved in two RAMs. Next, the rows of these saved data are moved back to 1D FFT block for second dimension computation of 2D FFT. As soon as the first valid output data are ready, computation of image reconstruction will be continued.

The internal control unit provides the address for RAMs to save resulted matrix of the first dimension of 2D FFT. In addition, it controls the activity of 1D FFT block. One reason to separate 2D FFT control unit from the main control unit in the architecture is to lower the load of the main control unit. Another reason is to make the control units simpler for design and optimization.

We used the Xilinx IP core [18] to calculate 1D FFT. Since 2D FFT of the 32×32 matrix should be calculated, and one column or row is operated at a time, transform length of this IP core is set
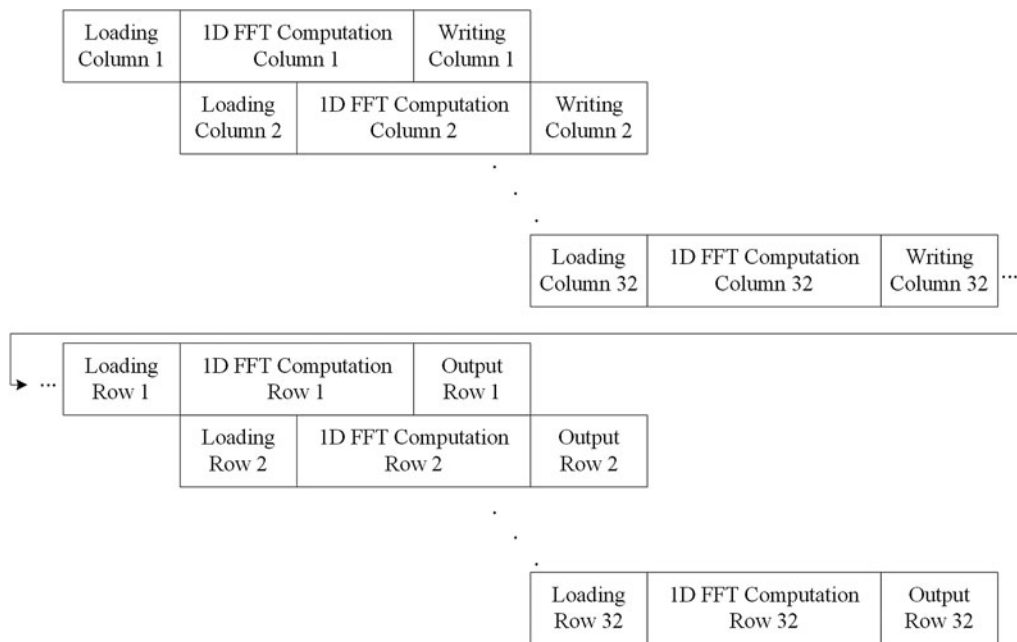
Fig. 25. 2D FFT unit operation.

to 32. This IP core has several implementation options. Pipelined streaming I/O option is selected, which allows continuous import of the input data to IP core, and continuous receive of output data. In addition, this core is preset to calculate FFT in fixed-point format.

Operation of 2D FFT is illustrated in Fig. 25. According to this figure, in the loading stage, each data are received continuously from the previous block with the rising edge of the clock signal. The processing matrix is 32×32, so each loading stage takes 32 clock cycles. It is reminded that these loading stages are exactly after each other, and there is no pause between them. As explained above, first the columns of the matrix are loaded and processed. Then, the rows of the resulted matrix are loaded to 1D FFT IP core. Next, the output data stream are sent to the next block for further computation. The number of clock cycles between the first input and its corresponding output is the latency in 1D FFT. This IP core is preset to produce outputs in a natural order, so only the number of clock cycles between the first input and first output can be considered as latency, which equals to 182 clock cycles as reported in the Xilinx core generator user guide.

Architecture operation

Operation of the proposed architecture is illustrated in Fig. 26 for one computation. Resource sharing technique utilization can be seen for RAMs block due to its operations in two different time slots. Disabling each block when it is idle is used in this architecture to reduce the power consumption. The architecture is truly parallel. For example, RAMs and the lookup table work parallel, also AGU, RAMs, the Lookup table and the complex multiplier executions have overlap with 2D FFT. Therefore, the produced data by these blocks are delivered directly to 2D FFT for processing the columns. Furthermore, again RAMs unit for the final frequency shift execution have overlap in time axis with 2D FFT row execution.

According to Fig. 26, L_1 to L_5 are latencies of each block, which are reported in Table 1. Total latency, which means when first
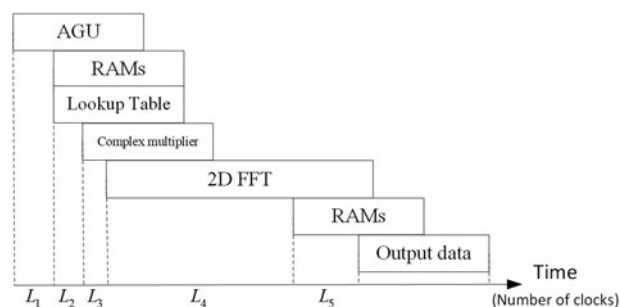

Fig. 26. The architecture operation.

valid data of the reconstructed image are shown in the output, is 1886 clock periods. Consequently, a complete image reconstruction for 32×32 input matrix needs 1886 plus 1024 periods of the clock that equals to 2910 clock periods.

Experimental results

Some experimental results of the proposed architecture are presented in this section. The proposed architecture is implemented on XC5VfX30 T VIRTEX-5 FPGA of Xilinx Corporation. Hardware resource consumption of FPGAs contains the number of slice registers, slice LUTs, occupied slices, memory usage, and DSP blocks. For 32×32 input matrix, utilized resources are presented in Table 2. Fixed-point number representation is used to perform arithmetic operations, and most operations are done using 12 bits as fraction. These 12-bit fractions are also used in 2D FFT calculation. Input raw hologram is an array of fixed-point numbers with 12-bit fractions.

Maximum clock frequency for the proposed architecture is 204.5 MHz, and this architecture was tested for 200 MHz clock frequency. Table 3 shows features of the computer for the performance measurement of the proposed architecture. The

Table 1. Latency of each block.

Latency	L_1	L_2	L_3	L_4	L_5	Total Latency
Number of clocks	8	2	3	1338	535	1886

Table 2. Slice logic utilization.

Slice logic utilization	Used
Number of slice registers	2658
Number of slice LUTs	1981
Number of occupied slices	1052
Total memory used (KB)	162
Number of DSP48Es	29

Table 3. Software development environment.

Windows 10 (64-bit)	OS
Intel(R) Core i7 7500U 2.9 GHz	CPU
8 GB	RAM
MATLAB	Programming language

Table 4. Supply power consumption for different clock rates.

Clock (MHz)		50	100	150	200
Supply power (mW)	Dynamic	113	164	232	425
	Quiescent	489	489	490	491
	Total	602	653	722	916

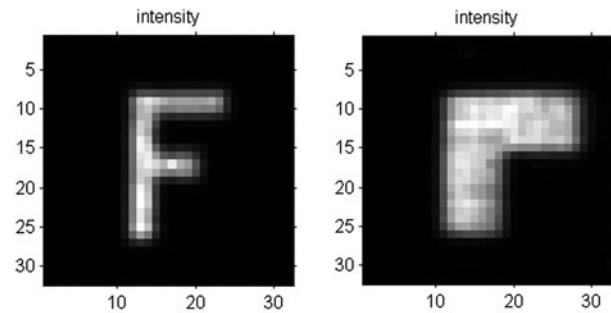**Fig. 27.** Reconstructed images by proposed hardware architecture (a) F shaped target (b) Γ shaped target.

proposed architecture resulted in approximately 30.5 times improvement in computation time compared to computer. The proposed hardware needs 14.55 µs for a complete image reconstruction, which is defined as the time between the start of computation and the time when the last data of the reconstructed image are produced in output. For the experiment, the clock rate is 200 MHz (i.e., the period is 5 ns).

Power consumption for one complete image reconstruction with proposed architecture is shown in Table 4 for different clock rates. Consumed power is estimated using XPower Analyzer, which is provided by Xilinx Company. This estimation was done for the ambient temperature of 25°C. It is observed from Table 4 that for 200 MHz clock frequency, the power consumption is 916 mW. In this clock frequency, quiescent power (also called static power) which includes the design and device static power (https://www.xilinx.com/support/documentation/sw_manuals/xilinx11/xpa_c_quiescent_power.htm) is 491 mW, and dynamic power is 425 mW. Additionally, a decrease in power consumption can be observed by clock rate.

The reconstructed images of the targets in Fig. 6 with the proposed hardware architecture are shown in Fig. 27. As can be seen, these images are similar to the reconstructed targets in Figs 7 and 8, which were reconstructed by MATLAB with infinite precision. It is crucial to know that how successfully the proposed architecture is able to reconstruct the image compared with infinite precision calculation, so a comparison based on [19] was performed. The image produced in MATLAB was the reference image for comparison with the reconstructed image by the proposed architecture. According to this comparison, it was shown that intensity matching for F and Γ shaped targets are 99.93 and 99.8%, respectively. The little decrease in matching is due to the reduction of fraction bits for performing calculations in the proposed architecture.

Conclusion

In this paper, an efficient Fresnel-based algorithm for single- and multi-frequency microwave imaging has been proposed. By neglecting the impact of target depth on image reconstruction, an efficient formula is developed, which only needs a single FFT to reconstruct the target image from the recorded raw data for both 2D and 3D microwave imaging. This reduces the computational load significantly compared with similar microwave imaging algorithms. Furthermore, a scanner using a PNA network analyzer and two nearby X-band antennas one as transmitter and the other one as receiver has been built for saving raw data. Several tests have been carried out to ensure the effectiveness of the algorithm. Copper, aluminum, and plastic targets have been used for this purpose. Finally, a prototype pipeline hardware was proposed to reduce the time of image reconstruction for the 2D algorithm. With a Clock frequency of 200 MHz, it shows a speed improvement of 30.5 times. Fixed-point representation was used for performing arithmetic operations due to its efficiency for FPGA resource utilization. Resulted images by this hardware were more than 99.8% similar to the corresponding images reconstructed by MATLAB.

References

1. **Narayanan RM, Wilson SA and Rangaswamy M** (2017) Sparsely Sampled Wideband Radar Holographic Imaging for Detection of Concealed Objects. *Progress in Electromagnetics Research B* **72**, 67–93.
2. **Sheen DM, McMakin DL and Hall TE** (2001) Three-Dimensional Millimeter-Wave Imaging for Concealed Weapon Detection. *IEEE Transactions on Microwave Theory and Techniques* **49**, 1581–1592.
3. **Ivashov SI, Razevig VV, Vasiliev IA, Zhuravlev AV, Bechtel TD and Capineri L** (2011) Holographic Subsurface Radar of Rascan Type: Development and Applications. *IEEE Journal of Selected Topics in Applied Earth Observations and Remote Sensing* **4**, 763–778.
4. **Sheen DM, McMakin DL, Collins HD, Hall TE and Severtsen RH** (1996) Concealed Explosive Detection on Personnel Using a Wideband Holographic Millimeter-Wave Imaging System. Paper presented at the Aerospace/Defense Sensing and Controls 2755, 503–513.

5. **Zhuravlev A, Bugaev A, Ivashov S, Razevig V and Vasiliev I** (2011) Microwave Holography in Detection of Hidden Objects under the Surface and beneath Clothes. Paper presented at the XXXth URSI General Assembly and Scientific Symposium, 1–4.

6. **Razevig V, Ivashov S, Vasiliev I and Zhuravlev A** (2012) Comparison of Different Methods for Reconstruction of Microwave Holograms Recorded by the Subsurface Radar. Paper presented at the Ground Penetrating Radar (GPR), 14th International Conference on, 335–339.

7. **Savelyev T and Yarovoy A** (2013) 3d Imaging by Fast Deconvolution Algorithm in Short-Range Uwb Radar for Concealed Weapon Detection. *International Journal of Microwave and Wireless Technologies* **5**, 381–389.

8. **Zhuravlev A, Ivashov S, Razevig V, Vasiliev I and Bechtel T** (2014) Inverse Synthetic Aperture Radar Imaging for Concealed Object Detection on a Naturally Walking Person. SPIE 9074.

9. **Yurduseven O** (2014) Indirect Microwave Holographic Imaging of Concealed Ordnance for Airport Security Imaging Systems. *Progress In Electromagnetics Research* **146**, 7–13.

10. **Sun Y, Hu W-D, Meng X-X and Lv X** (2015) 3-D near-Field Millimeter Wave Imaging Based on Stepped Frequency System. Paper presented at the Advanced Materials and Processes for RF and THz Applications (IMWS-AMP), IEEE MTT-S International Microwave Workshop Series on, 2015.

11. **Zhu Y-K, Yang M-H, Wu L, Sun Y and Sun X-W** (2016) Millimeter-Wave Holographic Imaging Algorithm with Amplitude Corrections. *Progress In Electromagnetics Research M* **49**, 33–39.

12. **Tan W, Huang P, Huang Z, Qi Y and Wang W** (2017) Three-Dimensional Microwave Imaging for Concealed Weapon Detection Using Range Stacking Technique. *International Journal of Antennas and Propagation* **2017**, 1–11.

13. **Bhatia R, Sharma AK and Saxena J** (2016) Improved Analysis of Four Wave Mixing with Sub-Plank Higher-Order Dispersion Parameters in Optical Communication Systems. *Optik* **127**, 9474–9478.

14. **Bhatia R, Sharma Ajay K and Saxena J** (2016) Comparative Investigations of DWDM Transmission System with PMD for Different Orthogonally Modulated Signals at 80 Gb/S. *International Journal of Communication Systems* **29**, 1084–1090.

15. **Schnars U and Jüptner W** (2005) *Digital Holography: Digital Hologram Recording, Numerical Reconstruction, and Related Techniques.* Germany: Springer-Verlag Berlin Heidelberg.

16. **Sakamoto Y, Tajiri K, Sawai T and Aoki Y** (1988) Three-Dimensional Imaging of Objects in Accumulated Snow Using Multifrequency Holography. *IEEE Transactions on Geoscience and Remote Sensing* **26**, 430–436.

17. **Zhuge X** (2010) *Short-Range Ultra-Wideband Imaging with Multiple-Input Multiple-Output Arrays* (Doctoral thesis). Department Electrical Engineering, Mathematics and Computer Science, TUDelf University, Delft, Netherlands.

18. xfft_ds260, LogiCORE IP Fast Fourier Transform v7.1 (2011) XILINX corporation.

19. **Wang Z, Bovik AC, Sheikh HR and Simoncelli EP** (2004) Image Quality Assessment: From Error Visibility to Structural Similarity. *IEEE Transactions on Image Processing* **13**, 600–612.

Farshad Zamiri received a B.S. degree in electronics engineering from Shahid Beheshti University, Tehran, Iran in 2015 and received his M.S. degree in Electronic Integrated Circuits from Tarbiat Modares University, Tehran, Iran in 2017. His main research interests are digital signal processing hardware design and design of microwave imaging systems.

Abdolreza Nabavi received the B.Sc. and M.Sc. degrees in Electrical Eng. from Tehran University, Tehran, Iran, in 1985 and 1987, respectively, and the Ph.D. degree in Electrical Engineering from McGill University, Montreal, Canada in 1993. Since 1993, he has been with the Faculty of Electrical and Computer Engineering, Tarbiat Modares University, Tehran, where he founded the Microelectronic Laboratory. From 2013 to 2014, he was with University of Waterloo, Ontario, Canada, as a visiting researcher working on MMIC design for Ka-band on-the-move satellite communications. His research interests include general area of VLSI with emphasis on basic logic circuits for low-voltage low-power applications, design of low power ADCs, DACs, low noise amplifiers, and signal processing units, the design of mixed analog-digital systems in deep submicron CMOS technology, and RFIC design with emphasis on mm-wave and Terahertz systems.